Water Science & Technology

IWA PUBLISHING

Water Science & Technology Vol 88 No 7, 1910 doi: 10.2166/wst.2023.313

Visible light-induced catalytic performance of composite photocatalyst synthesized with nanomaterials WO_3 and two-dimensional ultrathin g-C_3N_4

Dongmei Li [a,*], Wenxin Zhang[a], Yi Huang[b], Haoxuan Feng[c], Zilin Wang[a], Zhuohong Yang[a], Jingkai Chen[d], Xueqiang Zhang[a], Gangyi Zhang[a] and Yanbing Chen[a]

[a] Guangdong University of Technology, Guangzhou, Guangdong 510006, China
[b] Guangzhou Design Institute Group Co., Ltd, Guangzhou 510620, China
[c] Affiliated High School of South China Normal University, Guangzhou, Guangdong 510630, China
[d] Guangdong Ocean University, Zhanjiang, Guangdong 524088, China
*Corresponding author. E-mail: ldm108@gdut.edu.cn

DL, 0000-0003-1128-2931

ABSTRACT

To improve the visible light-induced catalytic activities of Ultrathin g-C_3N_4 (UCN), a promising photocatalyst WO_3/UCN (WU) was synthesized. Its visible light-driven photocatalysis performance was controllable by adjusting the theoretical mass ratio of WO_3/UCN. We have calibrated the optimal preparation conditions to be: WO_3/UCN ratio as 1:1, the stirring time of the UCN and sodium tungstate mixture as 9 h and the volume of concentrated hydrochloric acid as 6 mL which was poured into the mixture solution with an extra stirring time of 1.5 h. The optimal photocatalyst WU_{opt} had porous and wrinkled configurations. Its light absorption edge was 524 nm while that of UCN was 465 nm. The band gap of WU_{opt} was 2.13 eV, 0.3 eV less than that of UCN. Therefore, the recombination rate of photo-generated electron–hole pairs of WU_{opt} reduced significantly. The removal rate of WU_{opt} on RhB was 97.3%. By contrast, the removal rate of UCN was much lower (53.4%). WU_{opt} retained a high RhB removal rate, it was 5.5% lower than the initial one after being reused for five cycles. The photodegradation mechanism was facilitated through the strong oxidation behaviors from the active free radicals $\cdot O_2^-$, ·OH and h^+ generated by WUopt under the visible light irradiation.

Key words: optimal synthesis conditions, photocatalytic oxidation mechanism, photodegradation performance, rhodamine B, visible light-induced catalytic activity, WO_3/2-dimensional ultrathin g-C_3N_4 composite photocatalyst

HIGHLIGHTS

- A novel visible light-induced catalyst was gained with nano-WO_3 and ultrathin g-C_3N_4.
- WO_3/UCN had a low bandgap 2.13 eV and offered abundant radicals $\cdot O_2^-$, ·OH and $\cdot h^+$.
- Wrinkled, porous and ultrathin features led to a lower electron–hole recombining rate.
- The removal rate of WO_3/UCN on RhB reached 97.3% within 50 min while 53.4% for UCN.
- The removal rate of WO_3/UCN was stable and dropped by only 5.5% after reused five runs.

GRAPHICAL ABSTRACT

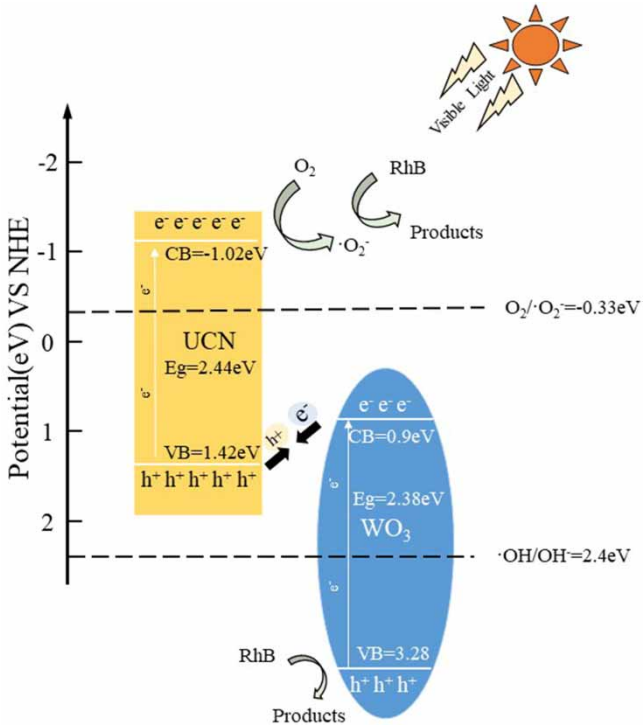

1. INTRODUCTION

Most of the organic pollutants (especially colored dye pollutants) in industrial wastewater are difficult to degrade, and it is difficult to meet the standards for drinking water through conventional or enhanced treatment processes (Brillas 2020). Colored dyes are mutagenic, carcinogenic and allergic (Dassanayake *et al.* 2018). Studies have shown that even wastewater containing only small amounts of dyes could seriously affect the growth of aquatic organisms (Garcia *et al.* 2021). Among them, most dyeing industries prefer to use cationic dyes. However, cationic dyes are more toxic than anionic dyes because of their aromatic ring structure of delocalized electrons and special synthetic methods (Doltabadi *et al.* 2016). Therefore, it has become a challenge to find ways to efficiently degrade cationic dyes (such as rhodamine B (RhB), methylene violet (MV) and methylene blue (MB)) with low cost and high efficiency in industrial wastewater (Cui *et al.* 2015).

There are several methods for the treatment of dye wastewater, including ion exchange, flocculating sedimentation (Doltabadi *et al.* 2016), advanced oxidation technology (Dassanayake *et al.* 2018; Nidheesh *et al.* 2018), activated carbon adsorption (Doltabadi *et al.* 2016) and biodegradation (Dhall *et al.* 2012). Some of these physical technologies (such as activated carbon adsorption and flocculating sedimentation) have significant treatment efficacy, but they only transfer organic dyes from the liquid phase to the solid one for separation, which causes serious secondary pollution. The biological treatment method is not suitable for the treatment of dye wastewater which has certain toxicity and is difficult to degrade. Advanced oxidation technology has drawn wide attention because it is a way to use some strong oxidizing active groups (such as hydroxyl radicals, sulfate radicals and so on) to oxidize and decompose organic pollutants to generate small molecules such as water and carbon dioxide (Nidheesh *et al.* 2018). The most commonly used advanced oxidation methods for the removal of organic dyes are mainly ozonation and Fenton methods, electrochemical oxidation and photocatalytic oxidation. Among them, the ozonation and Fenton methods have significant effects on the degradation of dyeing pollutants. However, it requires continuously adding oxidants to the wastewater, which increases the treatment cost. At the same time, a large amount of sludge is produced in the Fenton oxidation process, while the initial investment of ozonation is large and more undegradable substances may be generated during the degradation process (Wang *et al.* 2019). The electrochemical oxidation method has demonstrated advantages for treating dyes wastewater, such as the space-saving electrocatalytic device, high degradation efficiency and stable treatment effect. However, a lot of electric energy would be consumed in the process of

electrochemical reaction leading to a high processing cost. Furthermore, the electrode easily incurs side reactions such as hydrogen evolution, oxygen evolution and more.

The photocatalytic oxidation is one of the more advanced oxidation technologies. Its notable advantage is that photocatalysis is an efficient and environmentally friendly technology for the treatment of dyeing wastewater. However, ultraviolet photocatalytic energy consumption is huge which is hardly realistic in engineering applications (Dassanayake *et al.* 2018). Therefore, we grew an interest in the synthesis of catalysts responsive to visible light.

In recent years, the photocatalyst g-C_3N_4(CN) has drawn extensive attention from researchers because of its visible light-responsive performance, simple preparation methods, low price of raw materials and controllable electronic properties (Cui *et al.* 2020). CN is a type of two-dimensional (2D) polymer material mainly composed of carbon and nitrogen atoms. The band gap of CN prepared via the traditional thermal polycondensation method is around 2.6 eV. Compared with photocatalyst TiO_2, CN has a more active photocatalytic performance in the visible light range and a higher utilization rate of sunlight (Xu *et al.* 2016). However, CN still has some weaknesses, such as a small specific surface area, a severe recombination of photo-generated electron–hole pairs, poor dispersibility and a big band gap, which seriously confine its application in energy and environment (Pattnaik *et al.* 2019; Balakrishnan & Chinthala 2022).

In order to improve the visible light catalytic activity of CN, researchers have mainly reported two ways. One is to regulate the appearance of CN to synthesize ultrathin nanoplatelet g-C_3N_4 (UCN); the other is to construct heterojunctions with CN and metallic oxide. For the first way via regulating the appearance of CN to prepare UCN, many documents reported the improvement of its visible light catalytic activity. Lu *et al.* (2014) produced NH_3 by using ammonium chloride solid powder, and thermally exfoliated the bulk CN in an NH_3 atmosphere to prepare 2D nanoplatelet UCN with a specific surface area of 52.9 m^2/g, which was 19 times of bulk CN (2.9 m^2/g). Su *et al.* used the same method to prepare 2D nanoplatelet UCN. When the optimal dosage of 2D nanoplatelet UCN was 0.4 g/L, its degradation rate on enrofloxacin was 81.7% within 1 h, and its reaction rate constant was 4.1 times higher than that of bulk CN under visible light irradiation conditions (Su *et al.* 2017). The visible light-induced catalytic activity of 2D nanoplatelet UCN was enhanced significantly. The structure of the 2D ultrathin nanosheet accelerated the electron transmission rate in the photocatalytic process and reduced the recombination rate of photo-generated electron–hole pairs (Aggarwal *et al.* 2021). However, 2D nanoplatelet UCN still suffers from insufficient visible light absorption and rapid recombination rate of photo-generated electron–hole pairs. For the second way, it is to establish a heterojunction structure with two photocatalytic materials. The key point of constructing heterojunctions is to find two photocatalysts with matching energy bands, which can effectively improve the separation efficiency of photo-generated electron–hole, leading to a desirable visible light-responsive catalytic activity. Therefore, to improve the photocatalytic performance of CN via constructing heterojunctions with metallic oxide, the selection of metallic oxide is a top priority. There are many metallic oxides with different energy bands, such as WO_3 (2.4–3.2 eV), ZnO (3.12 eV), MnO_2 (3.36 eV), Fe_2O_3 (2.06 eV) and so on (Jung *et al.* 2018; Xia *et al.* 2018; Geng *et al.* 2021; Wang *et al.* 2023). WO_3 is a common semiconductor catalyst with a band gap of 2.4–3.2 eV, which can match that of CN. It can capture the blue light part of the solar spectrum and be considered as a promising photocatalyst (Aravindraj & Roopan 2022). The heterojunction composite photocatalyst WO_3/CN is formed by the staggered band arrangement between CN and WO_3 (Lou & Xue 2016). The WO_3/CN can effectively reduce the band gap and the recombination rate of photo-generated electron–hole pairs, which can improve the photocatalytic properties of CN and photodegradation performance on refractory organic matter. Zhang *et al.* (2021) synthesized CN/WO_3 composite photocatalyst via low-temperature template method. The specific surface area of CN/WO_3 was 54.8 m^2/g, 1.92 times that of CN. The photodegradation rate of CN/WO_3 was 4.27 times higher than that of CN. Wang *et al.* (2023) synthesized WO_3/CN photocatalyst via the hydrothermal method. Its band gap was 2.87 eV, and its photocatalytic activity was 6.4 times that of pure CN. Li & Du (2020) prepared composite photocatalyst WO_3/CN heterojunction by precipitation method and thermal polymerization. The degradation rate of WO_3/CN on Rhodamine B(RhB) reached 83% after 180 min of CN photocatalytic reaction. RhB was completely degraded when the WO_3/CN heterojunction kept reacting for 120 min. Nevertheless, the WO_3/CN heterojunction still has insufficient utilization of light energy and a high recombination rate of its photo-generated electron–hole pairs, which leads to a long photodegradation time, high energy gap or a low photodegradation rate.

According to the advantages and disadvantages of the prepared photocatalysts based on carbon nitride (CN) reported in the documents mentioned above, it was found that the photocatalytic performance of CN can be improved via regulating the appearance of CN to prepare UCN or synthesizing heterojunction with CN and WO_3. But even with this improvement, the enhancement of the active sites on its surface and visible light absorption capacity was still not sufficient.

Hence, it is possible to further improve the photocatalytic performance of CN to prepare a composite photocatalyst by making full use of the advantages of 2D nanoplatelet UCN and WO_3 having a matching energy gap and adjust their appearances to be more favorable for light adsorption. The composite photocatalyst had a higher photo-generated electron transmission than CN, which led to a decrease in the recombination rate of photo-generated electron–hole pairs.

In this study, the foaming agent ammonium chloride was used to synthesize 2D nanoplatelet UCN via thermal polycondensation method which was previously introduced (Li *et al.* 2022). On this basis, the composite photocatalysts WO_3/2D-UCN (WU) were synthesized with WO_3 and UCN at different theoretical mass ratios via the precipitation method. SEM, X-ray diffraction (XRD), scanning probe microscopy (AFM), X-ray photoelectron spectroscopy (XPS), ultraviolet-visible near-infrared spectroscopy (UV-vis) and photoluminescence spectroscopy (PL) were used to characterize WU and explore its photocatalytic properties with different theoretical mass ratios of WO_3 to 2D-UCN. Under visible light irradiation ($\lambda > 420$ nm), the photocatalytic degradation mechanism of WU and its degradation efficacy on typical cationic dye-Rhodamine B (RhB) was investigated.

2. MATERIALS AND METHODS

2.1. Experimental materials and reagents

Urea (CH_4N_2O), melamine ($C_3H_6N_6$) and ammonium chloride (NH_4Cl) were all analytically pure, and purchased from Shanghai Aladdin Biochemical Technology Co., Ltd. Sodium tungstate ($H_4Na_2O_6W$) was offered by Shanghai Macklin Biochemical Technology Co., Ltd, concentrated hydrochloric acid (HCl, purity of 35% (mass percentage concentration)) was purchased from Guangzhou Biotechnology Co., Ltd, anhydrous ethanol (C_2H_6O) was bought from Tianjin Damao Chemical Reagent Factory. All reagents were analytical grade.

2.2. Synthesis of 2D ultrathin nanoplatelet CN

2D-UCN was synthesized via the thermal polycondensation method. First, weigh 3 g of melamine, 3 g of urea and 10 g of ammonium chloride and dissolve them with 50 mL of ultrapure water in a crucible. Next, place the crucible in the water bath at 80 °C with a shaking intensity of 300 r/min till the mixture solution dried out. Afterwards, transfer the remained substance in the crucible to a muffle furnace (XS5-5-1200, Shenzhen Zhongda Electric Furnace Factory, 2016) at a heating rate of 1 °C/min to 550 °C for 3 h to gain UCN. Then, cool the UCN to room temperature (25 °C), grind and bag it for use. For comparative purposes, the bulk g-C_3N_4 (BCN) was prepared by repeating the above steps without adding ammonium chloride.

2.3. Synthesis procedure of composite photocatalyst WU heterojunction

The composite photocatalyst WO_3/UCN heterojunction (WU) was prepared via the precipitation method. First, weigh 200 mg of UCN and dissolve it in a beaker with 50 mL of ultrapure water and keep stirring at the speed of 300 r/min for 30 min to obtain UCN suspension. Next, disperse the suspension by ultrasonic apparatus (410HT, Shenzhen Jato Ultrasonic Cleaner Equipment. Co., Ltd, 2018) for 30 more minutes to obtain the UCN solution. Then, add 0.012 M of sodium tungstate solution dropwise to the UCN solution, disperse it uniformly by the ultrasonic apparatus for 1 h and put the beaker on a magnetic stirrer (89-2, Jintan Land Automation Instrument Factory, 2017) agitating for 9 h. Afterwards, add 6 mL of concentrated HCl into the beaker dropwise and keep stirring for 1.5 h. WU was collected by centrifugation of the mixture solution with sodium tungstate, UCN, concentrated HCl and ultrapure water mentioned above. Then washed WU several times with absolute ethanol and ultrapure water, respectively. The WU was dried at 90 °C overnight and ground into a fine powder for use. Finally, the composite photocatalysts were prepared under different conditions, changing the WO_3/UCN mass ratios, the stirring time, the amount of concentrated HCl, and the mixing time after adding concentrated HCl. The desirable heterojunction photocatalyst (WU_{opt}) was obtained at the optimum synthesis conditions which were determined via the orthogonal experimental design method.

2.4. Orthogonal experimental design

The synthesis conditions had an important impact on the photocatalytic performance of the visible light-induced catalyst WU heterojunction. The orthogonal test design method was adopted to determine the optimum synthesis conditions. In the orthogonal test design, L_n (f^m) was used to represent the effects of various factors, where f and m denote the number of levels and factors, respectively and n denotes the total number of experiments at different test conditions. The factors of the synthesis experiments included the dosage of two-dimensional Ultrathin g-C_3N_4 (for short UCN), the theoretical mass

ratio of WO_3 to UCN, the stirring time, the amount of concentrated HCl, the mixing time after adding concentrated HCl (denoted as M_{UCN}, M_{WO3}:M_{UCN}, t_1, V_{HCl}, t_2, respectively). Four levels were set for each factor. The evaluation index was set as the photodegradation rate (η) of RhB which was employed in the orthogonal test design to determine the optimal synthesis conditions of WO_3/UCN heterojunction.

The orthogonal test design consisted of several steps. First, a standard orthogonal test design table was selected. The 'factor' columns of the table were filled with their own levels. Next, experiments were conducted according to the orthogonal test design scheme. The test results were entered into the 'index' column in the L_n (f^m) format. Then, the sum (S) of each index value corresponding to the same level of each factor column was calculated. In addition, the average values of 'K' were gained through 'S' which were divided by the number of occurrences in each level. Finally, the extremum -"R' value, the difference between the maximum and minimum values of 'K', was determined. 'K' was applied to denote the optimum combination of factors corresponding to the optimal experimental conditions, and 'R' was used to evaluate the degree of influence of each factor on the photocatalytic properties of the visible light-induced catalyst WO_3/UCN heterojunction in the synthesis process. Higher values of 'R' were associated with higher levels of influence on an index.

Hence, the influence degree of each factor on the photocatalytic performance of the WO_3/UCN heterojunction was evaluated based on the value of 'R', and the optimum synthesis conditions of WO_3/UCN were determined accordingly. Then the optimal heterojunction WO_3/UCN (WU_{opt}) was applied to do tests.

2.5. The photocatalytic performance test procedure

For different photocatalysts UCN, WO_3, and WU, their photocatalytic degradation efficiencies on RhB were tested under visible light irradiation conditions. The first step was to prepare the simulated dyeing wastewater by taking RhB as a target pollutant in accordance with the procedure as below, for instance, weigh 1 g of RhB, dissolve it in ultrapure water and obtain RhB solution (1 g/L). The simulated RhB wastewater (20 mg/L) was prepared by diluting a small amount of stock solution (1 g/L). The second step was to conduct photocatalytic degradation experiments. First, add 50 mg of photocatalyst into the beaker with 50 mL of RhB solution and keep stirring (200 r/min) for 60 min at 25 °C under dark conditions to reach adsorption–desorption equilibrium. Afterwards, turn on the cooling circulating water device and place the mixture solution with RhB and photocatalyst under the irradiation of visible light (10 cm away from the liquid surface of the beaker) for photocatalytic degradation reaction. During the experiments, the illuminant was a 500 W xenon lamp (HF-GHX-XE-300, Shanghai Hefan Instrument Co., Ltd, 2019) and the ultraviolet light was filtered with a 420 nm filter. Next, the mixture solution samples were taken at 10 min intervals and filtered with a 0.22 μm filter, and then the absorbance of the solution was measured by UV-vis spectrophotometer ($\lambda = 554$ nm, UV-5100, Shanghai Yuanxi Instrument Co., Ltd, 2016). The properties of the photocatalysts aforementioned were tested by repeating the above experimental steps.

2.6. Test procedure of stability

To explore the stability of a photocatalyst, continuous cyclic degradation experiments were conducted. Once a photodegradation experiment of the photocatalyst (WU_{opt}) with optimum degradation efficiency at the visible light irradiation was complete, the used WU_{opt} was reclaimed by centrifugation and recovered for the second photodegradation experiment at the same conditions. This cycle was repeated five times for conducting photocatalytic degradation experiments of WU_{opt} on RhB. Its degradation rate was tested each time.

2.7. Test method of oxidative active species

In order to explore the photodegradation mechanism of the optimum catalyst WU_{opt}, it is significant to disclose the possible oxidative active species produced in the photocatalytic process. The capture experiments were conducted with the steps below. For instance, to take RhB as a dyeing pollutant, the photodegradation experimental reactor was placed under the illuminance of a 500 W xenon lamp (HF-GHX-XE-300, Shanghai Hefan Instrument Co., Ltd, 2019) and the ultraviolet light was filtered with a 420 nm filter. Next, three scavengers, such as ethylenediaminetetraacetic acid (EDTA, 2 mmol/L), p-benzoquinone (BQ, 1 mmol/L) and isopropanol (IPA, 10 mmol/L) were added into the reactor one by one under the visible light irradiation condition. The scavengers reacted with free possible radicals, such as hole (h^+), superoxide radical ($\cdot O_2^-$) and hydroxyl radical ($\cdot OH$). The photocatalytic degradation rate of WU_{opt} on RhB was tested accordingly.

3. RESULTS AND DISCUSSION

3.1. The optimal synthesis conditions

The orthogonal test design was conducive to determining the optimum synthesis conditions of the composite photocatalyst WO_3/UCN (WU). Five factors were selected below: UCN dosage (M_{UCN}), mass ratio of WO_3 to UCN (M_{WO3}:M_{UCN}), stirring time (t_1), concentrated hydrochloric acid volume (V_{HCl}) and mixing time after adding concentrated HCl (t_2). Four levels were set for each factor. According to the extremum R, the influence degree of each factor on photocatalytic performance was evaluated, which illustrated the optimal synthesis conditions of WU.

The orthogonal experimental results of the synthesis conditions on photocatalytic performance are shown in Table 1. The optimum synthesis conditions were determined based on the index-removal rate of photocatalysts on RhB (η). Higher values of R were associated with higher levels of influence on an index. For the five factors mentioned above, their corresponding R values were ranked in the sequence below (see Table 1), R-M_{WO3}:$M_{UCN} > R$-$t1 > R$-$M_{UCN} > R$-$t_2 > R$-V_{HCl}. It revealed that the mass ratio of WO_3 to UCN (M_{WO3}:M_{UCN}) has the strongest influence on the visible light-induced catalytic degradation performance of photocatalysts among the five factors, followed by t_1, M_{UCN} and t_2 while concentrated HCl volume (V_{HCl}) has the minimum impact.

Therefore, the influence degree of each factor on the removal rate of photocatalysts on RhB (η) was ranked as M_{WO3}:$M_{UCN} > t_1 > M_{UCN} > t_2 > V_{HCl}$. In addition, R-M_{WO3}:M_{UCN}, R-t_1 and R-M_{UCN} were significantly higher than R-t_2 and R-V_{HCl}, which disclosed that M_{WO3}: M_{UCN}, M_{UCN} and t_1 were the key factors influencing the photodegradation performance of visible light-responsive catalysts. 'K' was applied to represent the optimum combination of factors corresponding to

Table 1 | The orthogonal experimental design and the analysis results

	Influencing factors					
The sequence of the test	M_{UCN} (mg)	M_{WO3}:M_{UCN}	t_1 (h)	V_{HCl} (mL)	t_2 (h)	Removal rate η (%)
1	100	4:1	3	2	0.5	47.22
2	100	2:1	6	4	1	85.11
3	100	1:1	9	6	1.5	97.20
4	100	1:2	12	8	2	72.54
5	200	4:1	6	6	2	43.66
6	200	2:1	3	8	1.5	72.25
7	200	1:1	12	2	1	87.72
8	200	1:2	9	4	0.5	65.98
9	300	4:1	9	8	1	43.23
10	300	2:1	12	6	0.5	77.14
11	300	1:1	3	4	2	76.41
12	300	1:2	6	2	1.5	61.35
13	400	4:1	12	4	1.5	42.22
14	400	2:1	9	2	2	74.44
15	400	1:1	6	8	0.5	80.62
16	400	1:2	3	6	1	55.67
$K_1(\eta)$	75.52	44.08	62.89	67.68	67.74	
$K_2(\eta)$	67.40	77.24	67.69	67.43	67.93	
$K_3(\eta)$	64.53	85.49	70.21	68.42	68.26	
$K_4(\eta)$	63.24	63.88	69.90	67.16	66.76	
i_{max}	100 mg	1:1	9 h	6 mL	1.5 h	
R	12.28	41.41	7.32	1.26	1.50	

Note: The subscripts 1, 2, 3 and 4 of K are used to indicate the first, second, third and fourth levels of each factor. K_i refers to the arithmetic mean value of η of all tests when the factors in this column are at the i-th level; i_{MAX} is the optimal level, which refers to the level corresponding to the maximum value of K_1–K_4; R indicates the extreme value of K_1–K_4.

the optimal synthesis conditions. A smaller value of K was connected with a lower level of impact on an index. As shown in Table 1, the optimal levels of the five factors (M_{WO3}: M_{UCN}, M_{UCN}, t_1, V_{HCl} and t_2) in the orthogonal test were M_{WO3}: M_{UCN} 1:1, M_{UCN} 100 mg, t_1 9 h V_{HCl} 6 mL and t_2 1.5 h corresponding to their maximum K-value, respectively. Therefore, the optimal synthesis conditions of the desirable composite photocatalyst were determined as M_{WO3}: $M_{UCN} = 1{:}1$, $M_{UCN} = 100$ mg, $t_1 = 9$ h, $V_{HCl} = 6$ mL and $t_2 = 1.5$ h. The corresponding prepared composite photocatalyst was denoted as WU_{opt}.

3.2. Static adsorption and photodegradation property of WU_{opt}

In the dark condition, the photocatalyst WU_{opt} exhibited adsorption characteristics on RhB with consecutive stirring (200 r/min). When the run time was up to 30 min, the adsorption rate of WU_{opt} on RhB (13.7%) tended towards stability. Even though the run time lasted for another 30 min, the adsorption rate remained at 14.3% after 30 min, which demonstrated that the adsorption reached an equilibrium state around 30 min. Different photocatalysts have various photodegradation performances which can be demonstrated by its degradation efficacy on pollutants. When the visible light irradiation was on for 50 min, the removal rates of UCN, WO_3 and WU_{opt} on RhB were 53.4, 8.3 and 97.3% correspondingly (Figure 1(a)). WU_{opt} had the highest removal rate (97.3%). The rate constant (k) of RhB was fitted by the Langmuir–Hinshelwood first-order kinetic model, and the results are shown in Figure 1(b). The rate constant k of UCN and WU_{opt} were 0.01099 and 0.06778 min^{-1}, respectively. The latter was 6.12 times the former. The rate constant of WU_{opt} was the highest.

3.3. Phase structure characteristics

The phase structure of photocatalyst WU_{opt} was characterized by its atomic arrangement and periodicity which were analyzed via X-ray diffractometer (Bruke-D8, Germany, 2016). Figure 2 displayed the XRD patterns of UCN, WO_3 and WU_{opt}. UCN had a diffraction peak at $2\theta = 12.9°$ and 27.6°, corresponding to (100) and (002) crystal planes (Su *et al.* 2017). Characteristic diffraction peaks of WO_3 occurred in crystal planes (020), (111), (131), (202), (222) and (113), which were in line with the results in the standard card (JCPDS:No.84-0886) (Chen *et al.* 2019). For WU_{opt}, there were strong diffraction peaks at $2\theta = 12.9°$, 16.4°, 25.5°, 27.6°, 34.9°, 49.5°, 52.6°, 57.3° and no other impurity phase occurred (Figure 2). Therefore, it can be concluded that the composite photocatalyst WO_3/UCN (WU) was synthesized successfully.

3.4. Morphological structure characteristics of photocatalysts

The appearance and structure of the photocatalyst had a significant impact on its catalytic performance. Regulating its appearance was conducive to improving the catalytic properties. The morphological structure characteristics of photocatalysts UCN, WO_3 and WU_{opt} were analyzed using a field emission scanning electron microscope (LYRA 3, Tescan, Czech Republic, 2016). The scanning electron microscopy (SEM) images are shown in Figure 3(a)–3(d). UCN possessed lots of pores, which were created by many gases generated in the process of NH_4Cl calcination at high temperatures (Figure 3(a)).

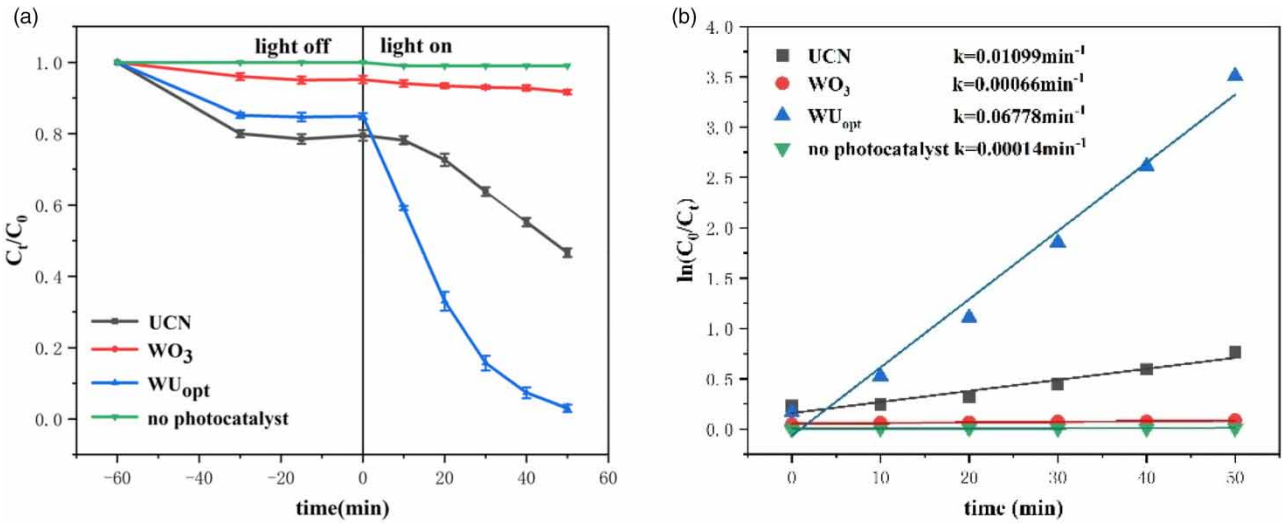

Figure 1 | The degradation rate of different photocatalysts on RhB (a) and the k-value fitting curve of the degradation rate (b).

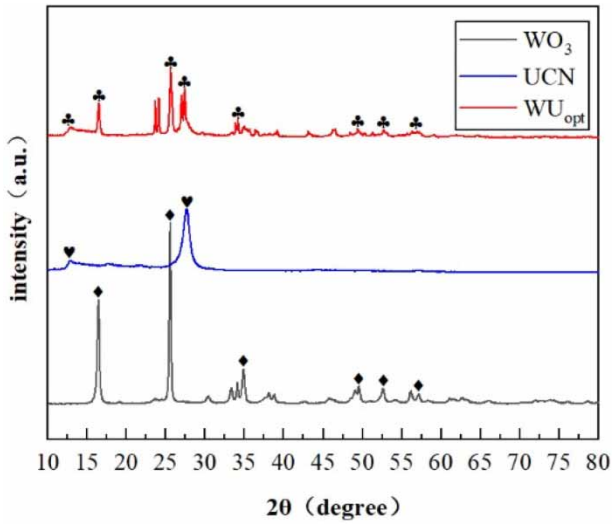

Figure 2 | XRD patterns of UCN, WO_3 and WU_{opt}.

The wrinkled and porous appearance promoted the adsorption capacity of UCN on pollutants because of its increased specific surface area. More importantly, this rough configuration with abundant porosity not only provided a large number of photocatalytic active sites but also guided the diffusely reflected incident light. Therefore, the utilization rate of light energy and the photocatalytic performance of UCN were enhanced (Lu *et al.* 2014; Liu *et al.* 2016; Su *et al.* 2017). WO_3 has presented uniformly sized and regular nanosheets (Figure 3(b)). The structure of the composite photocatalyst WU_{opt} was displayed in Figure 3(c) and 3(d) at different multiples. WO_3 platelets grew homogeneously on the surface of UCN and overlapping each other which caused WU_{opt} to have a wrinkled and porous appearance. Figure 3(d) at 10,000 multiples clearly demonstrated that WO_3 nanosheets in diameter around 200 nm were spread on the surface of UCN. The appearance of WU_{opt} was beneficial for the migration of photo-generated carriers in the band gap between WO_3 and UCN, which could improve its photocatalytic properties significantly.

The elemental contents of W, O, N and C in WU_{opt} were analyzed with the help of Energy Dispersive Spectroscopy (EDS), which are shown in Figure 3(e). The weight percentage (wt%) of the four elements are 28.99, 9.49, 33.92 and 27.60%, respectively (Table 2). The distribution of elements W, O, N and C in the photocatalyst WU_{opt} was uniform and WO_3 nanoparticles were homogeneously loaded on the surface of UCN nanosheets, which further confirmed the successful preparation of WU_{opt} heterojunction.

The thickness of UCN and WU_{opt} was characterized by means of atomic force microscopy (AFM). UCN and WU_{opt} had 2D ultrathin nanostructures with a thickness of 4–7 nm and 4–15 nm, respectively (Figure 4(a)–4(d)). The ultrathin nanostructure could accelerate the electron transport rate and reduce the recombination rate of photo-generated electron–hole pairs in the photocatalytic process, which was conducive to the improvement of photocatalytic activity (Aggarwal *et al.* 2021).

3.5. Photocatalytic activity comparison of visible light-induced composite catalysts

3.5.1. Visible light absorption capacity

Visible light absorption capacity is a significant factor for a photocatalyst to manifest the utilization rate of light energy and the photocatalytic efficiency. The higher the visible light absorption ability, the stronger the photocatalytic activity. UV–Vis diffuse reflectance spectroscopy (UV-3600, Shimadzu Corporation, Japan, 2017) was used to test the characteristic parameters, such as light absorption edge and band gaps. The light absorption performance of UCN, WO_3 and WU_{opt} are shown in Figure 5(a)–5(b). The light absorption edges of UCN, WO_3 and WU_{opt} were 465, 482 and 524 nm, respectively (Figure 5(a)).

The band gap can indicate the catalytic activity of the composite photocatalyst. A smaller band gap means a stronger light absorption capacity and a higher visible light catalytic activity. The band gaps of different composite photocatalysts were calculated with the Taucplot method. For UCN, WO_3 and WU_{opt}, their band gaps were 2.44, 2.38 and 2.13 eV, respectively

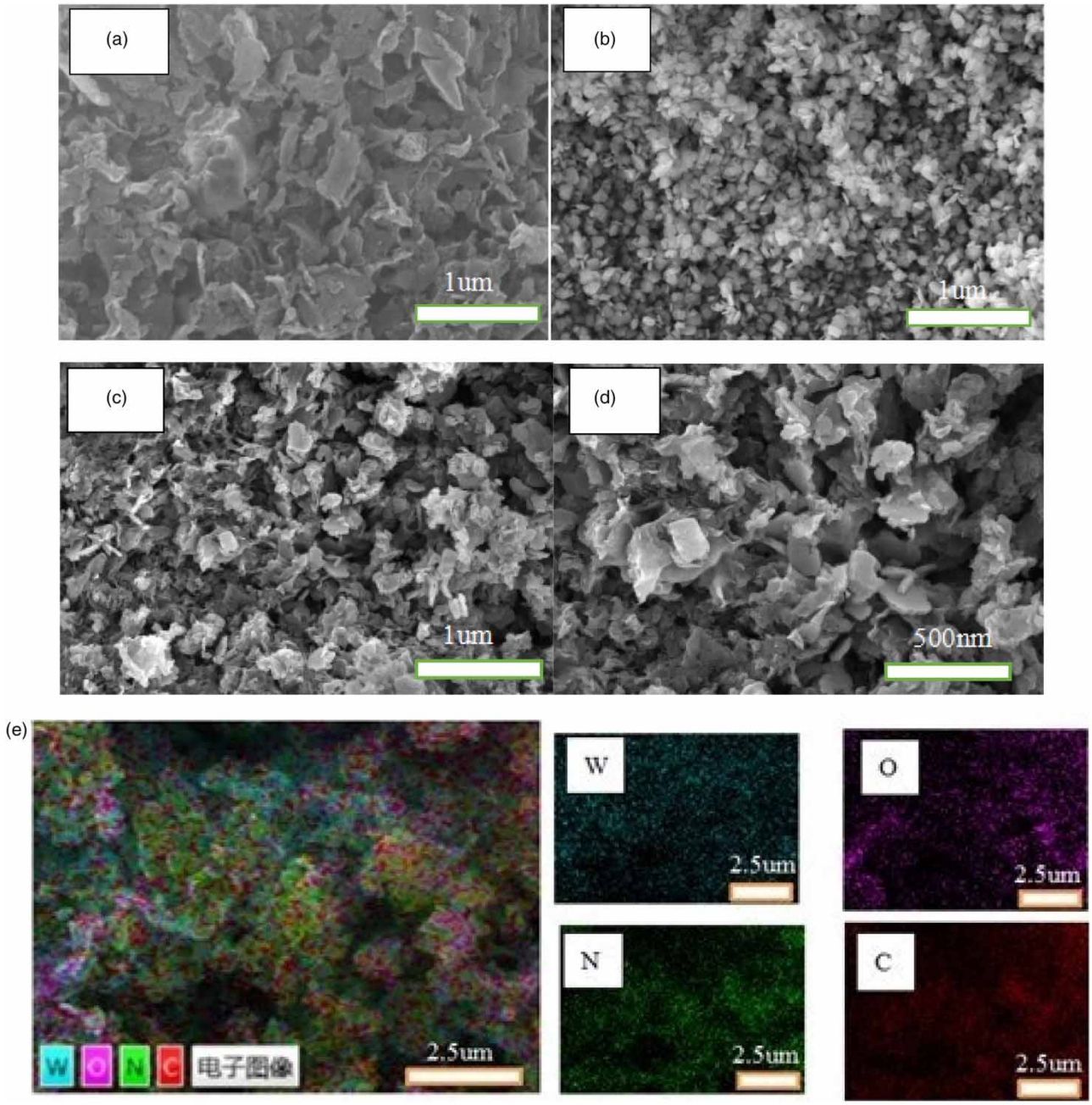

Figure 3 | (a) SEM images of UCN with magnification at ×5 k; (b) SEM images of WO_3 with magnification at ×5 k; (c) SEM images of WU_{opt} with magnification at ×5 k; (d) SEM images of WU_{opt} with magnification at ×10 k; and (e) EDS image of WU_{opt}.

(Figure 5(b)). Hence, the visible light absorption ability of composite photocatalyst WU_{opt} was much stronger than that of UCN. The synthesis of WU_{opt} with WO_3 and UCN led to a higher visible light catalytic activity.

3.5.2. Comparison of photo-generated electron and hole recombination rate

Typically, the intensity of the emission peak is positively correlated with the recombination rate of photo-generated electron–hole pairs. A weaker emission peak intensity means a lower recombination rate. Consequently, the utilization rate of light energy is high. The recombination rate of photo-generated electron–hole pairs was characterized via a fluorospectrophotometer (Fluorolog-3, HORIBA, USA 2017). In the wavelength range of 400–600 nm, the emission peaks of different

Table 2 | The elemental EDS analysis of WU_{opt}

Element	wt%	Atomic percentage
C	27.60	42.00
N	33.92	44.27
O	9.49	10.84
W	28.99	2.88
Total:	100.00	100.00

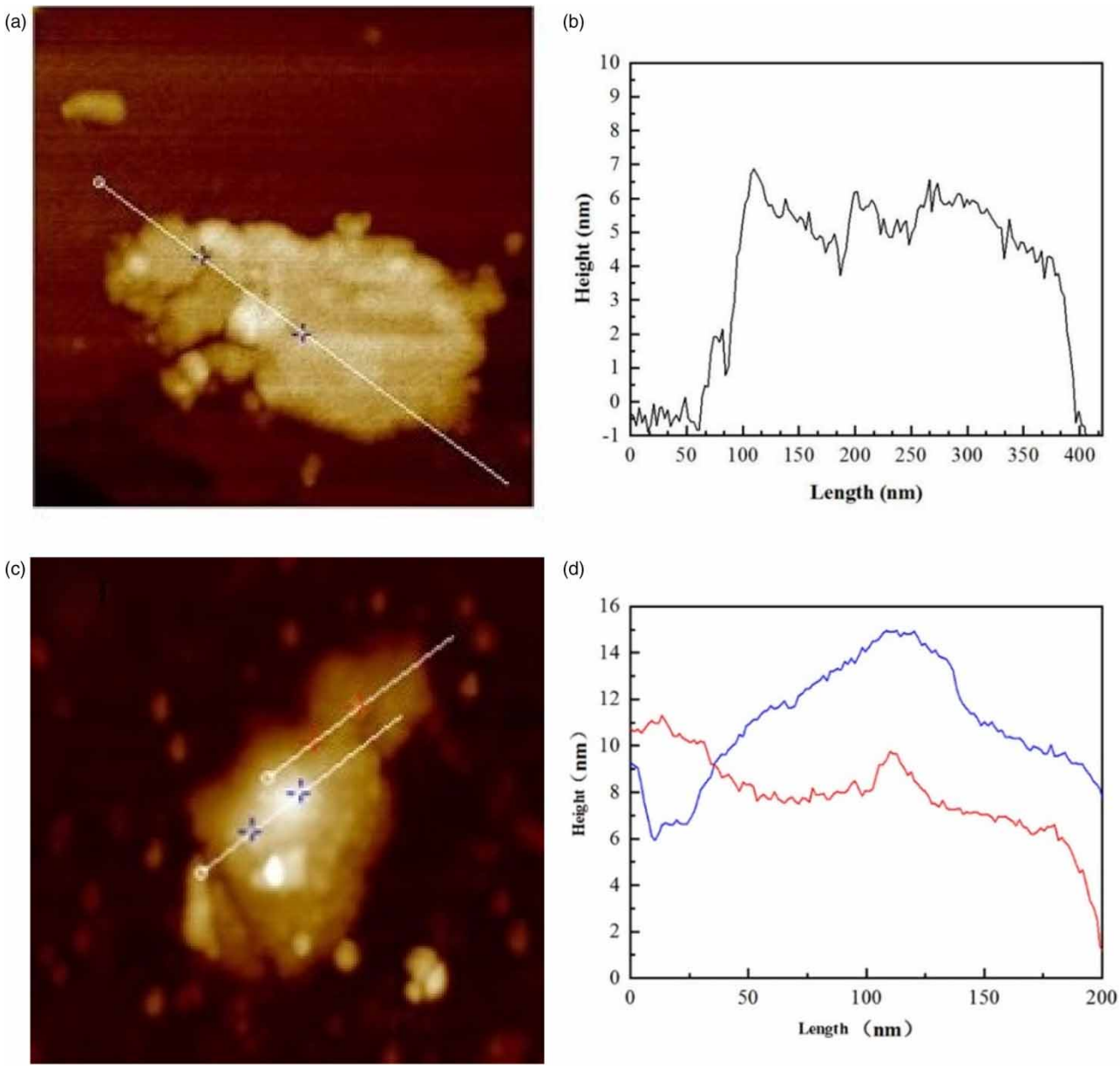

Figure 4 | (a) AFM image of UCN; (b) the height measurement results along the blue dotted white line in (a); (c) AFM image of UCN; (d) the height measurement results along the blue dotted white line and the red dotted white line in (c).

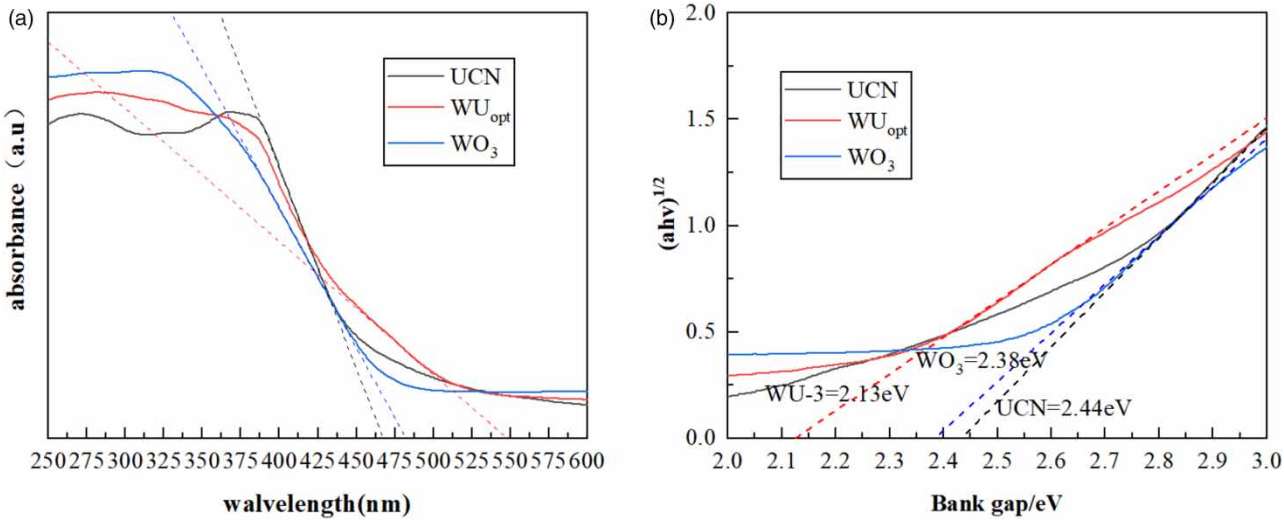

Figure 5 | (a) UV-vis DRS of UCN and WU_{opt}; (b) plots of the $(ahv)^{1/2}$ versus *hv* for UCN and WU_{opt}.

photocatalysts UCN and WU_{opt} had similar shapes. both emission peak intensities occurred at the same wavelength 460 nm. However, the emission peak intensity of WU_{opt} was much weaker than that of UCN (Figure 6). Therefore, WU_{opt} had a lower recombination rate which meant it had a stronger photocatalytic activity.

3.6. Element composition and valence characteristics of composite photocatalyst WU_{opt}

Elemental composition and valence characteristics could manifest the components and chemical properties of photocatalysts. X-ray photoelectron spectrometer (XPS, 250Xi, Thermo Fisher, USA, 2016) is helpful to analyze the element composition and valence characteristics of the composite photocatalyst WU_{opt}. The elements C, N, W and O were contained in WU_{opt} as expected, which revealed that the combination of WO_3 and UCN was successful (Figure 7(a)–7(d)). There were

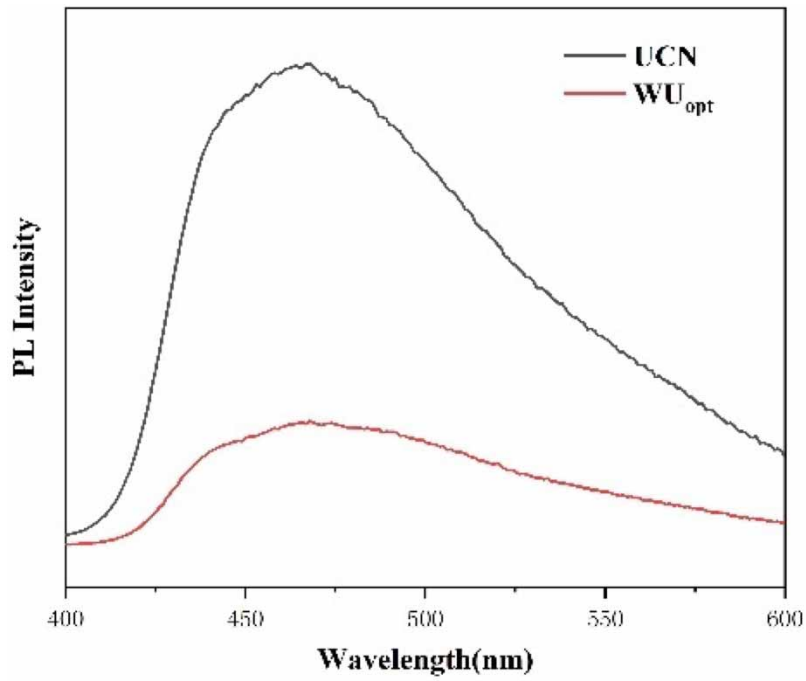

Figure 6 | PL spectra of different photocatalysts UCN and WU_{opt}.

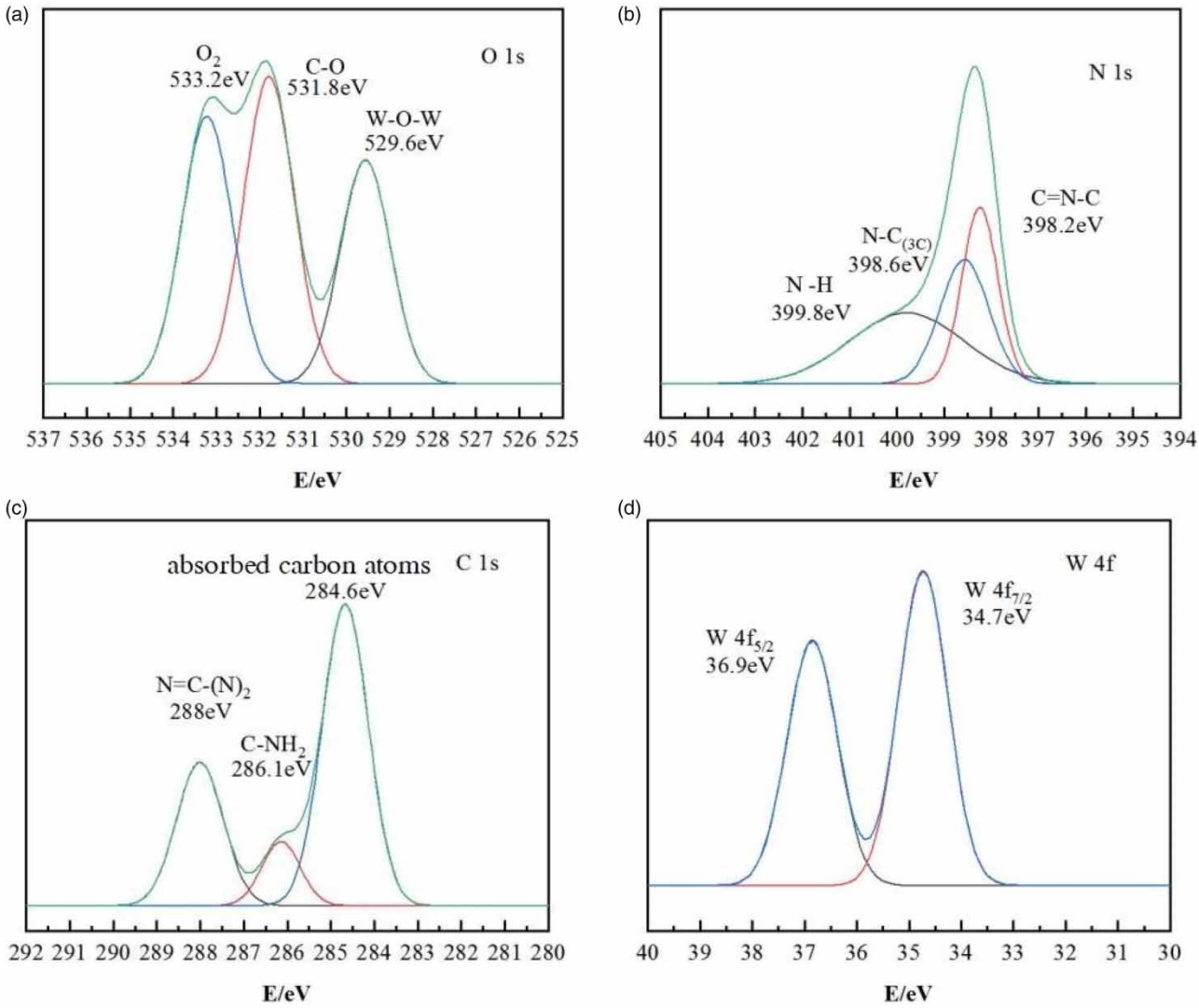

Figure 7 | XPS spectra of WU_{opt}, main peaks of O1s (a), N1s (b), C1s (c) and W4f (d) for WU_{opt}.

three forms of O element in WU_{opt} (Figure 7(a)), for example, O_2 on the surface of WU_{opt}, C = O in UCN and W–O–W in WO_3 at the binding energy of 533.2, 531.8 and 529.6 eV, respectively (Li & Du 2020). The N1s region was fitted into three main peaks by peak segmentation matching. They were N–H, N–C $_{(3C)}$ and C = N–C from UCN corresponding to the binding energy of 399.8.2, 398.6 and 398.2 eV separately (Figure 7(b)) (Yang *et al.* 2017). As shown in Figure 7(c), there were three forms of C element from UCN. They were $(N)_2$-C = N, C-NH_2 and the absorbed carbon atoms from outside pollution, which matched with the binding energy of 288, 286.1, and 284.6 eV, respectively (Yang *et al.* 2017). In addition, for the forms of W element in WU_{opt}, there were two main peaks representing $W4f_{7/2}$ and $W4f_{5/2}$ corresponding to the binding energy of 34.7 and 36.9 eV (Yu *et al.* 2017).

The XPS analysis results mentioned above manifested that WU_{opt} had demonstrated the valence characteristics of elements contained in UCN and WO_3. Therefore, it strongly proved that the WO_3/UCN was successfully prepared.

3.7. Visible light-responsive photodegradation stability and action mechanism

3.7.1. The stability of visible light-induced catalyst WU_{opt}

Visible light catalytic stability of WU_{opt} can be disclosed through multiple cycle tests. There were four degradation rates of WU_{opt} on RhB 97.3, 96.1, 94.9, 93.5 and 91.8% corresponding to five cycles of photodegradation experiments, respectively (Figure 8(a)). The removal rate of WU_{opt} dropped by only 5.5% after reusing five cycles which indicated that WU_{opt} had

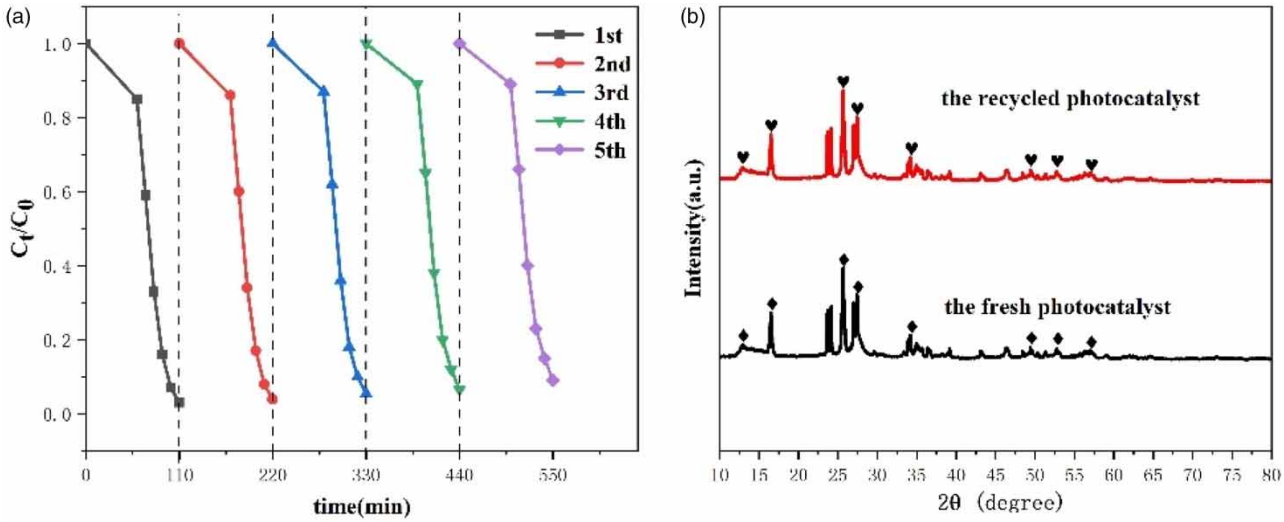

Figure 8 | (a) Photocatalytic performance test of WU_{opt} in the consecutive reused five cycles; (b) XRD patterns of WU_{opt} before and after photocatalytic reaction.

owned stable photocatalytic performance. The comparison of the XRD patterns of WU_{opt} before and after the photocatalytic reaction. The (100), (002), (020), (111), (131), (202), (222) and (113) diffractions were still maintained after the reaction, which proved that the WU_{opt} photocatalyst had high stability again (Figure 8(b)).

3.7.2. Action mechanism of photocatalyst WU_{opt}

The active free radicals play a main role in the photodegradation process. How to test the main types of active species is significant. They can be determined via free radical capture experiments. Effects of capture agents for different active species on the degradation rate of RhB are shown in Table 3. The photocatalytic degradation rate of WU_{opt} was only 2.1% after adding p-benzoquinone (BQ) which could capture the radicals $\cdot O_2^-$ (Table 3). In other words, the $\cdot O_2^-$ was the dominant active radical when the RhB was degraded. Likewise, after adding IPA and EDTA, the photocatalytic degradation rate of WU_{opt} on RhB was 49.3 and 76.2%, respectively, which revealed that $\cdot OH$ was also the main active radical whereas the oxidation ability of h^+ was negligible in the process of experiments.

As seen from section 3.5.1, the band gap (E_g) of UCN and WO_3 were 2.44 and 2.38 eV calculated by the Tauc Plot method. For UCN, the conduction band (E_{CB}, −1.02 eV) and valence band (E_{VB}, 1.42 eV) were determined from formula (1) and formula (2), respectively. For WO_3, the corresponding E_{CB} and E_{VB} were 0.9 and 3.28 eV calculated in the same way as that of UCN.

$$E_{CB} = X - E_C - E_g/2 \quad (1)$$

$$E_{VB} = E_{CB} + E_g \quad (2)$$

Table 3 | Capturing experiments of free radicals in the photocatalytic process of WU_{opt}

	SCAVENGER			
Serial number	**BQ**	**EDTA**	**IPA**	**RhB degradation rate (%)**
1	√			2.1
2		√		76.2
3			√	49.3
4				97.3

X is the absolute potential of the semiconductor, EC is the electron-free energy (about 4.5 eV) relative to the hydrogen potential level and E_g is the band gap of the semiconductor.

At the visible light irradiation, UCN and WO_3 can absorb light and be excited to generate photo-generated electron–hole pairs. For WO_3, since its E_{CB} (0.9 eV) was higher than the potential of O_2/O_2^- (−0.33 eV vs. NHE), the electrons on CB cannot reduce the dissolved oxygen in the system (Chen *et al.* 2019). However, for UCN, its E_{VB} (1.42 eV) had a lower energy level than the potential (+2.4 eV vs. NHE) of $\cdot OH/OH^-$, the photo-generated holes h^+ in the valence band (VB) cannot oxidize OH^- into $\cdot OH$ (Chen *et al.* 2019). The E_{CB} of UCN was more negative than the potential of $O_2/\cdot O_2^-$. The dissolved oxygen in the reaction system can be reduced to $\cdot O_2^-$ by accepting electrons of UCN. $\cdot O_2^-$ has high oxidizing properties and can degrade RhB. At the same time, the E_{VB} of WO_3 is more positive than the potential of $\cdot OH/OH^-$, so the h^+ on the VB of WO_3 can oxidize OH^- to $\cdot OH$. The photo-generated electrons excited on the conduction band (CB) of WO_3 nanosheets could be transferred to the VB of UCN, and the same photo-generated holes in the VB of UCN nanosheets also could be transferred to the CB of WO_3, which gained the effective separation of photo-generated carriers. This was consistent with the experimental results in the free radical capture experiment that $\cdot OH$ and $\cdot O_2^-$ were the main active species in the photodegradation reaction. Based on the above analysis, the composite photocatalyst WU synthesized with WO_3 and UCN via interfacial polymerization ultimately formed a *Z*-scheme photocatalytic heterojunction, as shown in Figure 9. Accordingly, more photo-generated holes combined with oxygen to produce photoactive species, which improved the degradation efficiency of WU_{opt} on RhB at visible light irradiation. The specific action mechanism and degradation process of the photocatalyst WU_{opt} on RhB are shown below.

$$WU_{opt} + hv \rightarrow h^+ + e^- \tag{3}$$

$$O_2 + 2e^- \rightarrow \cdot O_2^-(main) \tag{4}$$

$$\cdot O_2^- + e^- + 2hv \rightarrow H_2O_2 \tag{5}$$

$$H_2O_2 + e^- \rightarrow \cdot OH + OH^- \tag{6}$$

$$\cdot O_2^- + OH^- + RhB \rightarrow degraded\ mineralized\ products \tag{7}$$

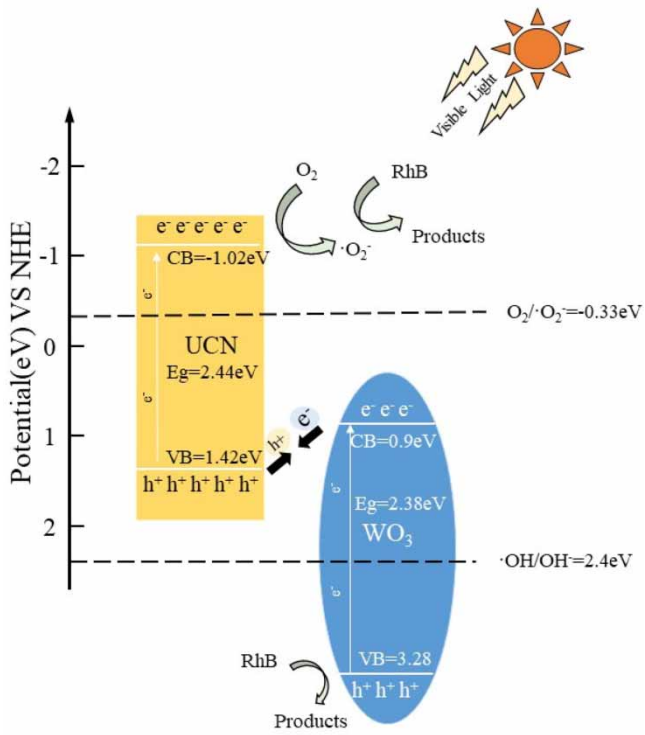

Figure 9 | The proposed photocatalytic mechanism of WU_{opt}.

4. CONCLUSIONS

A two-dimensional ultrathin carbon nitride g-C_3N_4 (UCN) was a new visible light-induced photocatalyst with a thickness of 4–7 nm. UCN was prepared by the foaming agent ammonium chloride via the thermal polycondensation method. By adding WO_3 to UCN, a noval promising composite catalyst WO_3/UCN(WU) with strong visible light-responsive photodegradation performance was gained via the precipitation method.

The optimal synthesis conditions were set as the theoretical mass ratio of WO_3 to UCN as 1:1, the stirring time of the mixture solution with UCN and sodium tungstate as 9 h, concentrated HCl as 6 mL which was poured into the mixture solution with an extra stirring time of 1.5 h. Under optimal conditions, the composite visible light-responsive catalyst WU has owned a satisfactory catalytic performance and multicycle photodegradation stability. WU_{opt} possessed a two-dimensional ultrathin structure with a thickness of 4–15 nm, which could accelerate the rate of electronic transmission and reduce the recombination rate of photo-generated electron–hole pairs. Besides, WU_{opt} had a wrinkled and porous appearance with a large number of active sites, conducive to incident light reflection and the utilization rate enhancement of light energy. WU_{opt} has presented broader infrared spectra than UCN. The light absorption edge of WU_{opt} was 524 nm while that of UCN was 465 nm. The band gap of WU_{opt} was 2.13 eV which was 0.3 eV less than that of UCN by characterization of UV-vis diffuse reflectance spectroscopy (DRS). Thus, the recombination rate of photo-generated electron–hole pairs of WU_{opt} decreased significantly. Taking advantage of the aforementioned characteristics, the optimal photocatalyst WU_{opt} exhibited about 2.1 times higher photocatalytic degradation efficiency on RhB (97.2%) within 50 min than that of UCN (only 53.4%). After being reused five cycles, WU_{opt} maintained a high RhB removal efficiency (91.8%) that was only 5.5% lower than that (97.3%) of the initial clean one.

The photodegradation mechanism of the novel composite photocatalyst WU_{opt} on RhB was that strong oxidation and degradation behaviors from the active free radicals $\cdot O_2^-$, $\cdot OH$ and h^+ were generated in the process of photocatalysis at the visible light irradiation. The active free radicals $\cdot O_2^-$ and $\cdot OH$ acted as a main role whereas h^+ was a negligible active substance in the photodegradation process.

ACKNOWLEDGEMENTS

The authors would like to thank the National Natural Science Foundation of China (Nos. 51378129 and 51108094) and the Natural Science Foundation of Guangdong Province (No. 2020A030313321) for their financial support.

DATA AVAILABILITY STATEMENT

All relevant data are included in the paper or its Supplementary Information.

CONFLICT OF INTEREST

The authors declare there is no conflict.

REFERENCES

Aggarwal, M., Basu, S., Shetti, N. P., Nadagouda, M. N., Kwon, E. E., Park, Y.-K. & Aminabhavi, T. M. 2021 Photocatalytic carbon dioxide reduction: exploring the role of ultrathin 2D graphitic carbon nitride (g-C_3N_4). *Chemical Engineering Journal* **425**, 131402.

Aravindraj, K. & Roopan, S. M. 2022 WO_3-based materials as heterogeneous catalysts for diverse organic transformations: a mini-review. *Synthetic Communications* **52**, 1457–1476.

Balakrishnan, A. & Chinthala, M. 2022 Comprehensive review on advanced reusability of g-C_3N_4 based photocatalysts for the removal of organic pollutants. *Chemosphere* **297**, 134190.

Brillas, E. 2020 A review on the photoelectro-Fenton process as efficient electrochemical advanced oxidation for wastewater remediation. treatment with UV light, sunlight, and coupling with conventional and other photo-assisted advanced technologies. *Chemosphere* **250**, 126198.

Chen, G. C., Bian, S. C., Guo, C. Y. & Wu, X. R. 2019 Insight into the Z-scheme heterostructure WO_3/g-C_3N_4 for enhanced photocatalytic degradation of methyl orange. *Materials Letters* **236**, 596–599.

Cui, H. J., Huang, H. Z., Yuan, B. & Fu, M. L. 2015 Decolorization of RhB dye by manganese oxides: effect of crystal type and solution pH. *Geochemical Transactions* **16**, 1–8.

Cui, S. C., Xie, B. W., Li, R., Pei, J. Z., Tian, Y. F., Zhang, J. P. & Xing, X. Y. 2020 g-C_3N_4/CeO_2 binary composite prepared and its application in automobile exhaust degradation. *Materials* **13**, 1274.

Dassanayake, R. S., Rajakaruna, E. & Abidi, N. 2018 Preparation of aerochitin-TiO_2 composite for efficient photocatalytic degradation of methylene blue. *Journal of Applied Polymer Science* **135** (8), 1–10.

Dhall, P., Kumar, R. & Kumar, A. 2012 Biodegradation of sewage wastewater using autochthonous bacteria. *Scientific World Journal* **2012**, 861–903.

Doltabadi, M., Alidadi, H. & Davoudi, M. 2016 Comparative study of cationic and anionic dye removal from aqueous solutions using sawdust-based adsorbent. *Environmental Progress & Sustainable Energy* **35** (4), 1078–1090.

Garcia, V. S. G., Tallarico, L. D. F., Rosa, J. M., Suzuki, C. F., Roubicek,D. A., Nakano, E. & Borrely, S. I. 2021 Multiple adverse effects of textile effluents and reactive Red 239 dye to aquatic organisms. *Environmental Science and Pollution Research* **28**, 63202–63214.

Geng, Y., Chen, D., Li, N., Xu, Q., Li, H., He, J. & Lu, J. 2021 Z-Scheme 2D/2D α-Fe_2O_3/g-C_3N_4 heterojunction for photocatalytic oxidation of nitric oxide. *Applied Catalysis B: Environmental* **280**, 119409.

Jung, H., Pham, T. T. & Shin, E. W. 2018 Interactions between ZnO nanoparticles and amorphous g-C_3N_4 nanosheets in thermal formation of g-C_3N_4/ZnO composite materials: the annealing temperature effect. *Applied Surface Science* **458**, 369–381.

Li, L. F. & Du, F. L. 2020 Synthesis of WO_3/g-C_3N_4 heterogeneous photocatalyst and degradation of dye wastewater. *Journal of Qingdao University of Science and Technology: Natural Science Edition* **41**, 35–42.

Li, D. M., Liu, X. Y. & Huang, Y. 2022 The synthesis of ultrathin heterojunction photocatalyst AgI/GO/g-C_3N_4 and its photocatalytic performance. *Acta Scientiae Circumstantiae* **42** (6), 90–100.

Liu, Q., Chen, T. X., Guo, Y. R., Zhang, Z. G. & Fang, X. M. 2016 Ultrathin g-C_3N_4, nanosheets coupled with carbon nanodots as 2D/0D composites for efficient photocatalytic H_2 evolution. *Applied Catalysis B: Environmental* **193**, 248–258.

Lou, Z. Z. & Xue, C. 2016 In situ growth of $WO_3 - x$ nanowires on g-C_3N_4 nanosheets: 1D/2D heterostructures with enhanced photocatalytic activity. *CrystEngComm* **18**, 8406.

Lu, X. L., Xu, K., Chen, P. Z., Jia, K. C., Liu, S. & Wu, C. Z. 2014 Facile one step method realizing scalable production of g-C_3N_4 nanosheets and study of their photocatalytic H_2 evolution activity. *Journal of Materials Chemistry A* **2**, 18924–18928.

Nidheesh, P. V., Zhou, M. & Oturan, M. A. 2018 An overview on the removal of synthetic dyes from water by electrochemical advanced oxidation processes. *Chemosphere* **197**, 210–227.

Pattnaik, S. P., Behera, A., Martha, S., Acharya, R. & Parida, K. 2019 Facile synthesis of exfoliated graphitic carbon nitride for photocatalytic degradation of ciprofloxacin under solar irradiation. *Journal of Materials Science* **54**, 5726–5742.

Su, Y. H., Wang, Y. F., Zhang, Q. X., Chen, T. S., Su, H. Y., Chen, P., Wang, F. L., Liu, H. J., Lu, W. Y., Yao, K. & Liu, G. G. 2017 The preparation of two-dimensional ultrathin g-C_3N_4 and the research of the photo-catalysis properties. *China Environmental Science* **37**, 3748–3757.

Wang, S., Wang, J., Wang, T., Li, C. & Wu, Z. 2019 Effects of ozone treatment on pesticide residues in food: a review. *International Journal of Food Science & Technology* **54** (2), 301–312.

Wang, X., Zhu, Z., Jiang, J., Li, R. & Xiong, J. 2023 Preparation of heterojunction C_3N_4/WO_3 photocatalyst for degradation of microplastics in water. *Chemosphere* **337**, 139206.

Xia, P., Zhu, B., Cheng, B., Yu, J. & Xu, J. 2018 2D/2D g-C_3N_4/MnO_2 nanocomposite as a direct Z-scheme photocatalyst for enhanced photocatalytic activity. *ACS Sustainable Chemistry & Engineering* **6** (1), 965–973.

Xu, J. H., Tan, L. H., Kou, B., Hang, Z. H., Jiang, W. & Jia, Y. Q. 2016 Modification of graphitic carbon nitride photocatalyst. *Progress in Chemistry* **28**, 131–148.

Yang, Y. X., Geng, L., Guo, Y. N., Meng, J. Q. & Guo, Y. H. 2017 Easy dispersion and excellent visible-light photocatalytic activity of the ultrathin urea-derived g-C_3N_4 nanosheets. *Applied Surface Science* **425**, 535–541.

Yu, W. L., Chen, J. X., Shang, T. T., Chen, L. F., Gu, L. & Peng, T. Y. 2017 Direct Z-scheme g-C_3N_4/WO_3 photocatalyst with atomically defined junction for H_2 production. *Applied Catalysis B: Environmental* **219**, 693–704.

Zhang, K., Jin, Y. & Guo, Y. 2021 Study on microstructure and photocatalytic mechanism of g-C_3N_4/WO_3 heterojunctions prepared by ice template. *ChemistrySelect* **6** (23), 5719–5728.

First received 11 August 2023; accepted in revised form 14 September 2023. Available online 28 September 2023